ARTICLE

Check for updates

Open-circuit voltage of organic solar cells: interfacial roughness makes the difference

Carl Poelking[1], Johannes Benduhn [2], Donato Spoltore [3], Martin Schwarze[2], Steffen Roland[4], Fortunato Piersimoni[4], Dieter Neher [4], Karl Leo[2], Koen Vandewal [3✉] & Denis Andrienko [1✉]

Organic photovoltaics (PV) is an energy-harvesting technology that offers many advantages, such as flexibility, low weight and cost, as well as environmentally benign materials and manufacturing techniques. Despite growth of power conversion efficiencies to around 19 % in the last years, organic PVs still lag behind inorganic PV technologies, mainly due to high losses in open-circuit voltage. Understanding and improving open circuit voltage in organic solar cells is challenging, as it is controlled by the properties of a donor-acceptor interface where the optical excitations are separated into charge carriers. Here, we provide an electrostatic model of a rough donor-acceptor interface and test it experimentally on small molecule PV materials systems. The model provides concise relationships between the open-circuit voltage, photovoltaic gap, charge-transfer state energy, and interfacial morphology. In particular, we show that the electrostatic bias generated across the interface reduces the photovoltaic gap. This negative influence on open-circuit voltage can, however, be circumvented by adjusting the morphology of the donor-acceptor interface.

mproving conversion efficiencies between photons and charges, phonons and charges[1], spins and charges[2], or triplet and singlet excitations[3] is a central target of contemporary energy research. For example, the understanding of the conversion pathways in organic solar cells led to a more than tenfold increase in power conversion efficiency (PCE)[4–15], with current non-fullerene-acceptor-based devices having nearly 19 % PCE [16,17].

Organic solar cells are actively studied due to their low cost, environmental friendliness, and ease of processing. In these cells, strongly bound excitons dissociate into charge-transfer (CT) states at donor–acceptor interfaces, which subsequently dissociate into free charge carriers, detected as photocurrent[5,18]. Early optimization strategies targeted materials with small optical and large photovoltaic gaps, defined as the difference between the ionization energy (IE) of the donor and electron affinity (EA) of the acceptor, $\Gamma = IE_D - EA_A$[19]. Small optical gaps helped to harvest a wider region of the solar spectrum, whereas larger photovoltaic gaps often correlated with larger open-circuit voltages, V_{oc}. It was, however, soon realized that the abstraction of the density of states of a heterojunction to a single photovoltaic gap is an oversimplification. Accounting for the broadening of energy levels motivated additional optimization strategies[20–23]. Furthermore, detailed macroscopic models pointed out the importance of the charge-carrier mobility and non-geminate recombination coefficient, thus providing optimization criteria for the thickness of the active layer in order to achieve high short-circuit currents and fill factors[24–27]. A whole new era in organic photovoltaic research started with the development of low-bandgap non-fullerene acceptors (NFAs)[11–15].

It was soon realized that long-range electrostatic interactions of a charge with surrounding molecular quadrupoles play a decisive role in defining the energetic landscape for electrons, holes and charge-transfer states[28–31]. The crystal field created by molecular quadrupoles contributes to the ionization energy (IE) and electron affinity (EA) of the organic film, and therefore to the open-circuit voltage of the solar cell[28]. This field also changes the energy offset between the charge-transfer and charge-separated states, favouring or disfavoring CT state dissociation[29,31–34]. It is unfortunate that the electrostatic effects, which favor efficient CT state dissociation also lead to a reduction of the photovoltaic gap, energy of the charge-transfer state, E_{ct}, and hence smaller V_{oc}. As a result, in order to optimize solar cell efficiency, one has to appropriately balance the electrostatic contributions to the energy profiles[32,33].

In this paper, we use tailored material systems in order to disentangle the effects of morphology, molecular and device architecture on the microscopic energetics. In the first set of experiments, we study planar heterojunction solar cells. While the acceptor phase is always C_{60}, the donor phase of these cells is a mixture of chemically similar compounds, $ZnPc:F_4ZnPc$ or $ZnPc:F_4^*ZnPc$, isomers of which are shown in Fig. 1. Due to fluorination, the quadrupole component along the normal of the molecular plane, $Q_{20} \equiv Q_{\pi\pi}$, differs significantly for all three compounds. This difference allows us to accurately tune the electrostatic field in the intermixed crystalline phase. As a result, IEs and EAs of such mixtures can be continuously tuned, while the crystalline morphology of the donor phase is preserved[31,35]. In the second set of experiments, an additional *mixed* donor:acceptor interlayer is deposited between the pure donor and acceptor layers. This interlayer is used to control the roughness of the donor–acceptor interface. We then show theoretically and prove experimentally that interfacial electrostatics can be used to tune the open-circuit voltage of an organic solar cell—by adjusting the roughness of the donor–acceptor interface. Moreover, we provide a detailed microscopic description of how V_{oc}, Γ,

and E_{ct} depend on system composition, interface roughness, and energetic disorder.

Results

Ionization energy and photovoltaic gap. We begin by analyzing the density of states (DOS) of intermixed $ZnPc:F_4ZnPc$ and $ZnPc:F_4^*ZnPc$ co-crystals. In the absence of intermolecular interactions, the DOS of the binary mixture would only consist of two peaks corresponding to the ionization energies of $ZnPc$ and F_4ZnPc (or $ZnPc$ and F_4^*ZnPc) in the gas phase, IE_0. The composition dependence of the IE and EA is thus given solely by the solid-state contribution $\Delta_h(c)$ for holes and $\Delta_e(c)$ for electrons, $IE(c) = IE_0 + \Delta_h(c)$, $EA(c) = EA_0 + \Delta_e(c)$, where c is the fraction of $ZnPc$ in the mixture.

The microscopic mechanism responsible for this dependence is the long-range superposition of quadrupolar fields that act on the charge carrier[31,35]. $ZnPc$ carries a net-negative out-of-π-plane quadrupole component, larger in magnitude than the corresponding negative quadrupole moment of F_4^*ZnPc, whereas the corresponding quadrupole component of F_4ZnPc is positive. In fact, this can be anticipated from the isopotential maps of the compounds, which are shown in Fig. 1. The long-range character of the charge-quadrupole interaction effectively results in a concentration-weighted average over both contributions, which can be used to tune ionization potential and electron affinity. This microscopic view is indeed supported by the good agreement between ionization energies measured by UPS[31,35] and simulated using atomistically resolved models, as shown in Fig. 2.

To relate this composition dependence of the energetics of holes in the mixtures to photovoltaic observables, we first consider its effect on the photovoltaic gap $\Gamma(c) = IE_D(c) + EA_A = \Gamma_0 + \Delta_{h,D}(c) + \Delta_{e,A}$. Here, $\Gamma_0 = IE_{0,D} + EA_{0,A}$ is the sum of the gas-phase IE of the donor and EA of the acceptor. $\Delta_{e,A} \simeq 0.95$ eV for C_{60} denotes the solid-state correction to electron site energies in the acceptor component, as calculated from atomistic models. Note that we define the photovoltaic gap based on the mean of the *low*-energy Gaussian mode within the bimodal density of states of the mixed $ZnPc:F_4ZnPc$ and $ZnPc:F_4^*ZnPc$ systems. This low-energy contribution is due to the $ZnPc$ component, and will eventually determine the chemical potential μ_h. The composition dependence of $\Gamma(c)$ is therefore inherited directly from $\Delta_{h,D}(c)$. As a result, $\Gamma(c)$ should display the same linear behavior in c as $IE_D(c)$.

Electrostatic interfacial bias. To quantify the electrostatic heterogeneity of the donor–acceptor interface, we define an *interfacial electrostatic bias* for holes and electrons, $B_h = \Delta_{h(A)} - c_1\Delta_{h,D_1} - c_2\Delta_{h,D_2}$, $B_e = c_1\Delta_{e(D_1)} + c_2\Delta_{e(D_2)} - \Delta_{e,A}$, where $\Delta_{h(A)}$ is the solid-state contribution to the ionization energy of the donor molecule in the acceptor mesophase, i.e., when the donor molecule is completely surrounded (perfectly dispersed) by C_{60}. Similarly, $\Delta_{e(D)}$ is this contribution to the electron affinity of the acceptor molecule placed in the donor mesophase. As the donor mesophase is a mixture of two compounds, we weigh the corresponding contributions of D_1 and D_2 by their respective concentrations in the mixture. In other words, if D_1 is $ZnPc$ then $c_1 = c$ and $c_2 = 1 - c$. In an ordered thin film, the solid-state contribution to the ionization energy and, therefore, the interfacial bias, are proportional to the $Q_{\pi-\pi}$ component of the quadrupolar quadripolar tensor[31,33]. For the columnar molecular arrangement shown in Fig. 2, $Q_{\pi-\pi} \equiv Q_{20}$ is the component of the tensor perpendicular to the conjugated core, as shown in Fig. 1.

B_h and B_e quantify the electrostatic asymmetry of the interface by comparing the external contributions for holes and electrons on the donor and acceptor side of the interface. They are defined
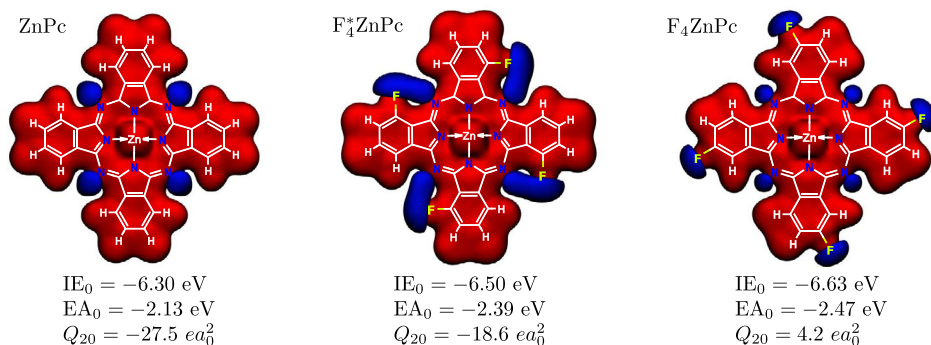
Fig. 1 Chemical structures and electrostatic surface potentials illustrating their distinct electrostatic architecture. Isopotential surfaces at -0.5 V and $+0.5$ V are shown in blue and red, respectively. Note that for F_4ZnPc, the material used is a mixture of different isomers, as the fluorine atoms can be in either of the two outer positions. IE_0 and EA_0 are gas-phase ionization energy and electron affinity, respectively, calculated at the B3LYP/6-311+g(d,p) level of theory. Q_{20} is the component of the quadrupole tensor in the direction normal to the molecular plane.
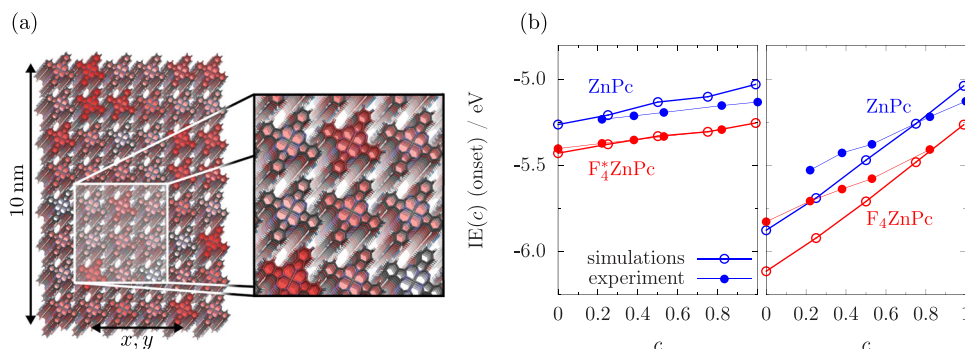

Fig. 2 Crystalline morphologies and corresponding ionization potentials. a Model of a crystalline binary $ZnPc:F_4ZnPc$ thin film, with species represented by (semi-transparent) and gray molecules, with periodicity in the xy plane. Deeper red implies more F_4ZnPc molecules in a column. **b** Dependence of the ionization energy (IE) on the fraction of ZnPc in the $ZnPc:F_4ZnPc$ and $ZnPc:F_4^*ZnPc$ systems, c.
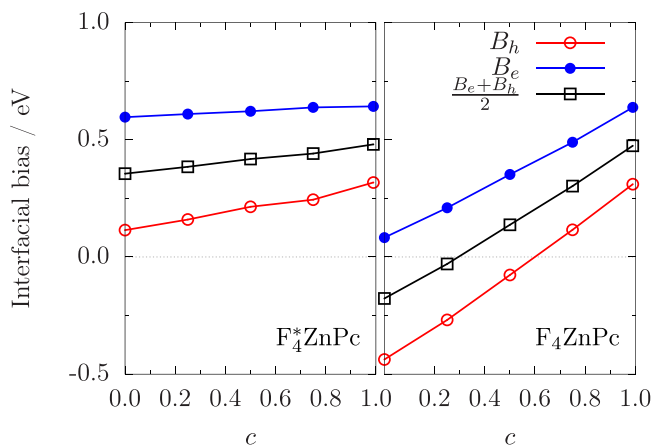

Fig. 3 Interfacial bias potential. Dependence of the interfacial bias potential for electrons (blue curves, filled circles) and holes (red curves, open circles) on the composition of the donor layer, c, for the $ZnPc:F_4ZnPc$ and $ZnPc:F_4^*ZnPc$ systems as obtained through simulations. The bias potential has a linear dependence on c, inherited from the solid-state contributions Δ_h and Δ_e to electron and hole site energies.

such that a positive interfacial bias pushes charge carriers away from the interface. To evaluate these quantities, we would need to explicitly simulate the donor–acceptor mixture. Instead, we approximate the corresponding solid-state contributions with their bulk values, $\Delta_{h(A)} \approx \Delta_{h,A}$ and $\Delta_{e(D)} \approx \Delta_{e,D}$. This approximation is reasonable at the donor–acceptor interface, where donor (acceptor) molecules have mostly donor (acceptor) nearest

neighbors, and where the long-range charge-quadrupole interactions dominate the solid-state contribution.

Since the solid-state contributions to the electron and hole on the donor side are linear in c, the interfacial bias also linearly depends on the composition, as shown in Fig. 3. Remarkably, for F_4ZnPc, B becomes negative at $c \simeq 0.3$, which is also where the fill factor of the solar cell starts to deteriorate, see Table 1. This can be rationalized in that a negative B, i.e., a negative bias for charge push-out, leads to trap formation at donor/acceptor sites that protrudes into the opposite (acceptor/donor) domain. The electrostatic bias of the F_4^*ZnPc system is always positive. This cell indeed performs much better than the F_4ZnPc device.

Charge-transfer states. We now evaluate the energies of interfacial CT states. Generally speaking, the energy of these states can be written as

$$E_{ct}(c) = \Gamma(c) - |\Delta_{eh}| + \chi(c, \rho). \quad (1)$$

Here, $|\Delta_{eh}|$ is an effective binding energy that results from the electron-hole attraction reduced by dielectric solvation[29,30,33,36]. This binding energy can be assumed to be independent of composition, and amounts to 0.5 eV for the closest CT states in results obtained through simulations[29,33]. $\chi(c, \rho)$ is the interfacial electrostatic bias, as discussed below.

The ionization energy and electron affinity are impacted by the interfacial morphology at the nanoscale[29,37]. At a *rough* interface, donor molecules or domains can protrude into the acceptor phase. As a result, their gas-phase energy levels are dressed by the electrostatic field of the acceptor phase. This superposition of electrostatic fields in the donor and acceptor films across an

Table 1 Summary of the measurements for the ternary cells. For ZnPc:F$_4^*$ZnPc/C$_{60}$ and ZnPc:F$_4$ZnPc/C$_{60}$ as well as the planar junction cell with an interlayer we report short-circuit currents, J_{scr}, open-circuit voltages, V_{ocr}, fill factors, power conversion efficiencies (PCE), charge-transfer energies E_{ct} and the corresponding fit parameters, as described in the "Methods" section.

| System	Thickness [nm]	J_{sc} [mA/cm^2]	V_{oc} [V]	FF [%]	PCE [%]	E_{ct} [eV]	λ [eV]	f [10^{-4}(eV)^2]
ZnPc/ C$_{60}$	10/40	3.33	0.47	66.4	1.04	1.08	0.24	0.50
ZnPc:F$_4^*$ZnPc (3:1) / C$_{60}$	10/40	3.17	0.48	63.3	0.97	1.13	0.34	2.54
ZnPc:F$_4^*$ZnPc (2:1) / C$_{60}$	10/40	3.18	0.48	65.2	1.00	1.13	0.35	2.35
ZnPc:F$_4^*$ZnPc (1:1) / C$_{60}$	10/40	3.14	0.51	65.0	1.03	1.16	0.41	5.63
ZnPc:F$_4^*$ZnPc (1:2) / C$_{60}$	10/40	3.09	0.53	65.3	1.06	1.20	0.50	19.4
F$_4^*$ZnPc / C$_{60}$	10/40	2.90	0.60	64.8	1.13	1.41	0.34	72.4
ZnPc/C$_{60}$	10/40	3.60	0.41	65.0	0.95	1.06	0.28	0.78
ZnPc:F$_4$ZnPc (3:1) / C$_{60}$	10/40	3.78	0.49	66.7	1.24	1.11	0.31	1.15
ZnPc:F$_4$ZnPc (2:1) / C$_{60}$	10/40	3.79	0.53	67.5	1.37	1.13	0.34	1.57
ZnPc:F$_4$ZnPc (1:1) / C$_{60}$	10/40	3.68	0.61	68.7	1.54	1.19	0.24	0.54
ZnPc:F$_4$ZnPc (1:2) / C$_{60}$	10/40	3.44	0.67	68.7	1.28	1.28	0.30	2.42
F$_4$ZnPc / C$_{60}$	10/40	1.78	0.89	36.9	0.59	1.49	0.18	7.89
ZnPc/ ZnPc:C$_{60}$ (1:1) / C$_{60}$	10/2/40	3.63	0.47	65.37	1.11	1.10	0.29	1.86
ZnPc/ ZnPc:C$_{60}$ (1:1) / C$_{60}$	10/4/40	4.15	0.49	66.30	1.36	1.16	0.35	16.8
ZnPc/ ZnPc:C$_{60}$ (1:1) / C$_{60}$	10/6/40	4.62	0.52	67.02	1.60	1.17	0.33	23.9
ZnPc/ ZnPc:C$_{60}$ (1:1) / C$_{60}$	10/8/40	5.07	0.53	67.23	1.79	1.17	0.32	31.7
ZnPc/ ZnPc:C$_{60}$ (1:1) / C$_{60}$	10/10/40	5.57	0.52	66.56	1.91	1.17	0.32	42.4
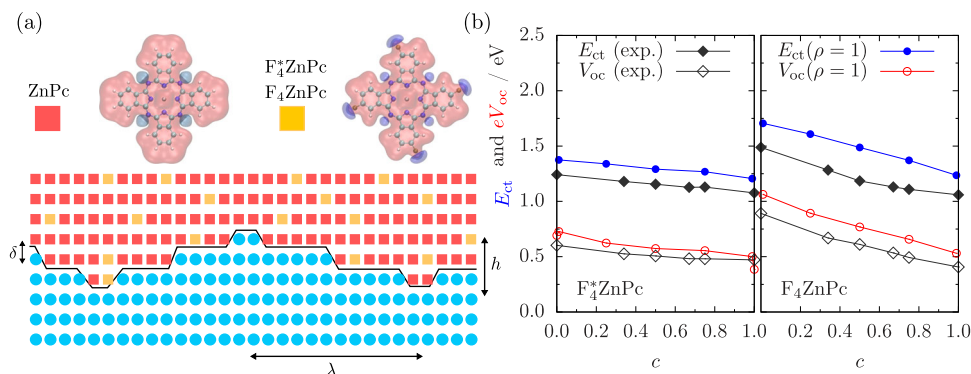
Fig. 4 Open-circuit voltage and charge-transfer state energy of a planar junction solar cell. a Model of a planar junction solar cell with a rough interface and co-deposited donor materials. Geometrical parameters of a rough interface: period, λ, width, h, and a minimal separation between the donor and acceptor molecules, δ. **b** Dependence of the open-circuit voltage (V_{oc}, open symbols), and charge-transfer state energy (E_{ct}, closed symbols) on the concentration c of ZnPc in the ZnPc:F$_4$ZnPc and ZnPc:F$_4^*$ZnPc solar cells. The experimentally measured slopes (black lines and symbols) are best reproduced for $\rho = 1$.

intermixed region is triggered by the same long-range mechanism that gives rise to the composition dependence of site energies in the mixed donor phase.

The degree of interface roughness determines to what extent this bias actually impacts the CT energy of interfacial donor–acceptor pairs. In Supplementary Note 2 we quantify the amount by which E_{ct} is raised ($B > 0$) or lowered ($B < 0$) by the bias for a rough interface of width h, which is shown in Fig. 4(a),

$$\chi(c, \rho) = \frac{1}{2}\left(B_e(c) + B_h(c)\right)\frac{\rho}{1+\rho}. \qquad (2)$$

In the limit where the corrugation period λ of the profile significantly exceeds both the depth h of the intermixed region, and the interlayer spacing δ, the degree of nanoscale roughness can be captured by a single parameter $\rho = 2h/\delta$.

To validate this relation, the measured composition dependence of E_{ct} is shown in Fig. 4b. Experimental details are provided in the Methods section and Table 1. The slope is best fitted with $\rho = 1$, which corresponds roughly to two intermixed molecular layers. As we will see in the next section, the same roughness is required to fit the dependence of the open-circuit voltage on the composition of the donor. Moreover, we will also show that the

interface roughness can be systematically varied in planar junction solar cells with an interlayer between the two phases.

Open-circuit voltage. With Γ and E_{ct} at hand, the composition-dependent open-circuit voltage, $V_{oc}(c) = \mu_e(c) - \mu_h(c)$ is calculated by evaluating the chemical potentials $\mu_e(c)$ and $\mu_h(c)$ of electrons and holes, respectively:

$$eV_{oc}(c) \simeq \Gamma(c) + \alpha k_B T \ln\left[n(c)p(c)\right] - \beta k_B T \hat{\sigma}^2(c), \qquad (3)$$

where $\alpha \approx 1$ and $\beta \approx 1/2$ are parameters with a weak dependence on charge density; $\hat{\sigma} = \sigma/k_B T \lesssim 5{-}6$ is the effective disorder strength of the donor (energetic disorder in the acceptor is negligible in the case of C$_{60}$), and n and p are the steady-state number densities (number of charges per number of available sites) of electrons and holes, respectively. The derivation is provided in Supplementary Note 1.

Evaluating n and p requires the simulation of the full dynamics of charge generation and recombination in a solar cell. Here, however, we are only interested in how the film composition affects V_{oc}. We therefore define n_0 and p_0 as the charge-carrier densities that would follow from an effectively zero electron-hole binding energy of CT states, and assume $n_0 = p_0 = 5 \times 10^{-6}$, as
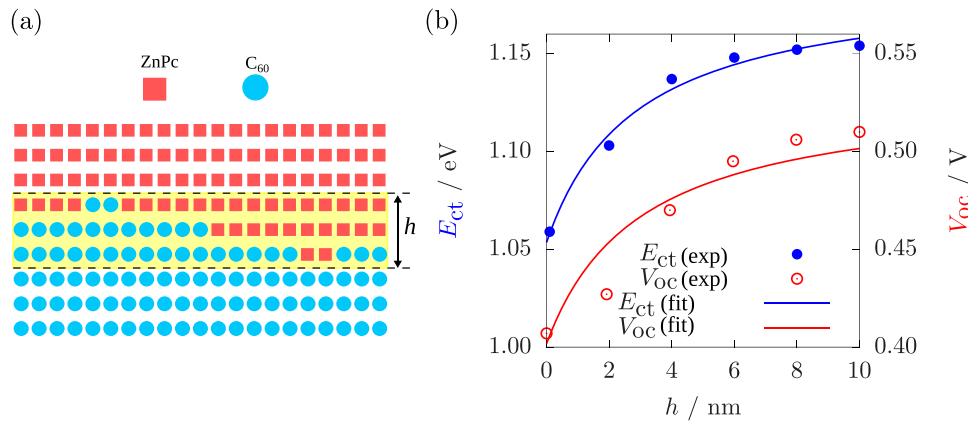
Fig. 5 Charge-transfer state energy and open-circuit voltage dependence on interfacial roughness. a Co-deposited layer of ZnPc:C_{60} sandwiched between pristine ZnPc and C_{60} layers. **b** Variation of the charge-transfer (CT) energy (E_{ct}, blue curve and filled symbols) and open-circuit voltage (V_{oc}, red curve and open symbols) with interface roughness, represented here by the interlayer thickness h. Dots are measurements performed on planar heterojunction cells with a ZnPc/ZnPc:C_{60}/C_{60} architecture. Solid lines are fits to Eqs. (6) and (3), with fit parameters $E_{ct,0} = 0.92$ eV, $\chi_0 = 0.27$ eV, $\delta = 1.43$ nm and $h_0 = 1.43$ nm and the $E_{ct} - eV_{oc}$ offset $\alpha k_B T \ln(n_0 p_0) = -0.66$ eV. These fitted parameters are in very good agreement with the values predicted by simulations, as well as the interface roughnesses extracted from the composition-dependent measurements in Fig. 4.

was found to accurately describe the V_{oc} under AM1.5g conditions of well-functioning systems with $B_h, B_e > 0$[29]. The steady-state charge-carrier densities can then be related to the charge push-out forces via a law of mass action, $np = n_0 p_0 \exp\left[-\frac{|\Delta_{eh}| - \chi_e(c,\rho) - \chi_h(c,\rho)}{k_B T}\right]$ and the open-circuit voltage is obtained as

$$eV_{oc}(c,\rho) \simeq \alpha E_{ct}(c,\rho) + (1-\alpha)\Gamma(c) + \alpha k_B T \ln[n_0 p_0] - \beta k_B T \hat{\sigma}^2(c), \quad (4)$$

where we have explicitly labeled the dependence on both composition c and roughness ρ. This relationship can finally be expressed in terms of the effective push-out energies $\chi_e + \chi_h = \chi$ simply via

$$eV_{oc}(c,\rho) = eV_{oc}(c,\rho = 0) + \alpha \chi(c,\rho). \quad (5)$$

Two important observations to be made here are as follows: first, as $E_{ct}(c,\rho = 0) + \alpha \Delta \chi(c,\rho)$ is the CT energy in the presence of charge push-out, the above relationship preserves correlations between the CT energy and V_{oc}. Second, it adequately captures its low-temperature extrapolation, $V_{oc} \to E_{ct}$ for $k_B T \to 0$ (for $\alpha \simeq 1$), in agreement with previous studies[38,39].

The measured open-circuit voltages as a function of composition are shown in Fig. 4. Note that the red (V_{oc}) and blue (E_{ct}) lines are not fits but theoretical predictions based on the expressions for $E_{ct}(c)$ and $\Gamma(c)$, Eqs. (1) and (5). The solid curves correspond to a surface roughness of $\rho = 1$, in which case the slope reproduces the experimental trends for both V_{oc} and E_{ct}. Note that here the increase in V_{oc} is correlated with the decrease in J_{sc}. This anticorrelation is due to the reduction of the driving force required to convert excitons into chare transfer states, or transfer the hole from the acceptor to the donor[32,33].

Of particular interest for solar-cell design is the correlation between the interfacial bias B and the open-circuit voltage. Due to symmetries of the electrostatic interaction sums for electrons and holes, the change of B and Γ with composition is anticorrelated: $\Delta B = -2\Delta\Gamma$. Meanwhile, $\Delta\chi \leq \Delta B/2$, as follows from Eq. (2). Two extremal situations can therefore be distinguished: (1) $\rho \sim 0$ (flat interface), where the change in open-circuit voltage follows precisely the change in photovoltaic gap, and (2) $\rho \gg 1$ (rough interface), where the change in the photovoltaic gap may be completely compensated by the change in charge-carrier density,

thus effecting an approximately constant V_{oc}. In systems such as ZnPc/C_{60} with $B > 0$, interface roughness is therefore advantageous in that it enhances V_{oc}, whereas it will be harmful in systems with $B < 0$, notably F_4ZnPc/C_{60}.

This conclusion can also be validated experimentally. To this end, we prepared planar heterojunction solar cells with an interlayer of mixed ZnPc:C_{60} (1:1). By changing the thickness h of this interlayer, we effectively modify the roughness ρ of the donor–acceptor interface (as indicated by in situ evaporation studies[40]), and thus the CT state energy:

$$E_{ct}(h) = E_{ct,0} + \frac{\chi_0}{1 + \frac{\delta}{h+h_0}}. \quad (6)$$

$E_{ct,0}$ here denotes the CT state energy in the absence of any interface roughness, $\chi_0 = (B_e + B_h)/2$ is the interfacial bias for the F_4ZnPc/C_{60} system, δ is the center-of-mass distance between C_{60} and F_4ZnPc in an edge-on orientation, and h_0 is the interfacial roughness of the planar heterojunction with $h = 0$, i.e., without mixed interlayer. The experimentally measured E_{ct} and V_{oc} dependencies are shown in Fig. 5 (symbols) and are in excellent agreement with the trends suggested by Eqs. (6) and (3): This is illustrated by the fitted solid lines, which correspond to $E_{ct,0} = 0.92$ eV, $\chi_0 = 0.27$ eV and $\rho = \delta/h_0 = 1$. These are in turn very close to the simulated values ($E_{ct,0} = 1.1$ eV, $\chi_0 = 0.48$ eV), while the surface roughness estimated from the fit agrees well with the earlier observation that $\rho \simeq 1$ also yields the best agreement between simulated and experimental trends in the composition-dependent setting, shown in Fig. 4.

Conclusions

To conclude, our model of a rough donor–acceptor interface accounts for the bending of the electrostatic potential and accurately captures the correlations between molecular architecture, film composition and open-circuit voltage. The linear dependence of the photovoltaic gap and charge-transfer state energies on composition is driven by the superposition of quadrupolar fields of ZnPc, F_4ZnPc, and F_4^*ZnPc. The same superposition creates a composition-dependent electrostatic bias at the donor–acceptor interface. A positive interfacial bias helps to split charge-transfer states and avoid non-geminate recombination. As, however, the change of the photovoltaic gap and electrostatic interfacial bias with composition are anticorrelated, $\Delta B \sim -2\Delta\Gamma$, an increased bias reduces the open-circuit voltage: For a perfectly planar

interface, the change in voltage follows precisely the change in photovoltaic gap. The reduction of the open-circuit voltage that follows from a large positive bias can be avoided at interfaces with nanoscale roughness. In ZnPc/C_{60} and F_4^*ZnPc/C_{60} with $B > 0$, interface roughness is advantageous in that it recovers the V_{oc} and suppresses charge recombination, whereas it is harmful in F_4ZnPc/C_{60} with $B < 0$.

Methods

Simulations. The microscopic calculations were performed on atomistic models of mixed ZnPc:F_4ZnPc and ZnPc:F_4^*ZnPc films of 10 nm thickness. Each thin-film layer consists of 17×6 molecules in an edge-on orientation as suggested by X-ray diffraction studies[41]. The intermixing of the two species is performed randomly, with the concentration of ZnPc denoted by c.

To appropriately model long-range effects in the energy calculations, periodic boundary conditions are used in the plane of the film, without, however, replicating the molecular excitation, or its polarization cloud. Based on this long-range embedding approach[37], we obtain the perturbative corrections $\Delta_{h,D}$ to hole (h) energy levels in the donor (D) film. The ionization energy (IE) results as $IE = IE_0 + \Delta_{h,D}$, where IE_0 denotes the IE of the respective compound in the gas phase[30]. All calculations were performed using the VOTCA package[42,43].

Sensitive EQE_{PV} measurements. The measurements were performed according to previous works, reproduced here for completeness[44].

The light of a quartz halogen lamp (50 W) is chopped at 140 Hz and coupled into a monochromator (Cornerstone 260 1/4m, Newport). The resulting monochromatic light is focused onto the organic solar cell (OSC), its current at short-circuit conditions is fed to a current pre-amplifier before it is analyzed with a lock-in amplifier (7280 DSP, Signal Recovery, Oak Ridge, USA). The time constant of the lock-in amplifier was chosen to be 1 s and the amplification of the pre-amplifier was increased to resolve low photocurrents. The EQE_{PV} is determined by dividing the photocurrent of the OSC by the flux of incoming photons, which was obtained with a calibrated silicon (Si) and indium-gallium-arsenide (InGaAs) photodiode.

Electroluminescence measurements were obtained with an Andor SR393i-B spectrometer equipped with a cooled Si and cooled InGaAs detector array (DU420A-BR-DD and DU491A-1.7, UK). The spectral response of the setup was calibrated with a reference lamp (Oriel 63355). The emission spectrum of the OSCs was recorded at different injection currents, which correspond to applied voltages lower than or at least similar to the V_{oc} of the device at 1 sun illumination.

The low-energy tail of the EQE_{PV} spectrum is fitted with a Marcus equation[38]

$$EQE_{PV}(E) = \frac{f}{E\sqrt{4\pi\lambda k_B T}} \exp\left[\frac{-(E_{ct} + \lambda - E)^2}{4\lambda k_B T}\right] \quad (7)$$

to obtain the charge-transfer state energy E_{CT}, the relaxation energy λ, and the oscillator strength f.

In cases where E_{ct} is close to the optical E_{opt} of the donor and accordingly no distinct CT state absorption is observed, E_{ct} was obtained by fitting the high energy tail of the EL spectra[38].

Device preparation. The devices were fabricated according to our previous work. The description is reproduced here for completeness[45]. All devices investigated in this work are constructed by a thermal evaporation vacuum system with a base pressure of less than 10^{-7} mbar. Before deposition, ITO substrates (Thin Film Devices Inc., USA) are cleaned for 15 min in different ultrasonic baths with NMP solvent, deionized water, and ethanol, followed by O2 plasma for 10 min. The organic materials are purified 1 or 2 times via thermal sublimation.

A first hole transporting layer is evaporated, consisting of 20 nm 9,9-*bis*[4-(N,N-*bis*-biphenyl-4-yl-amino)phenyl]-9H-fluorene (BPAPF) (Lumtec, Germany) doped at 10 wt% with NDP9 (Novaled, Germany). Subsequently, the active layer is evaporated. It comprises 10 nm of a blend of zinc-phthalocyanine (ZnPc) (ABCR, Germany) and tetrafluoro-zinc-phthalocyanine (F_4^*ZnPc) (BASF, Germany) or F_4ZnPc (synthesized by Dr. Beatrice Beyer, Fraunhofer FEP, Dresden) in varying ratios, from pure ZnPc to pure F_4^*ZnPc or F_4ZnPc (see main text for more information). An additional layer of ZnPc and Buckminster Fullerene (C_{60}) (CreaPhys, Germany) in a 1:1 weight ratio is evaporated, the thickness is varied from 0 to 10 nm. Afterward a 40 nm C_{60} layer is evaporated. The devices are finalized with 8 nm of Bathophenanthroline (BPhen) (Lumtec, Germany), used as electron contact, and finished with 100 nm of Al. The devices are defined by the area overlap of the bottom and the top contact with an active area of 6.44 mm^2. To avoid exposure to ambient conditions, the organic part of the device is covered by a small glass substrate, glued on top utilizing an epoxy resin (Nagase ChemteX Corp., Japan) cured by UV light. To hinder degradation, a moisture getter (Dynic Ltd., UK) is inserted between the top contact and the glass.

Current–voltage characteristics. Current–voltage characteristics are measured with a SMU (Keithley 2400) at standard testing conditions (16 S-150 V.3 Solar Light Co., USA) with a mismatch corrected light intensity and under dark conditions. All results are summarized in Table 1.

Data availability
The datasets generated during and/or analyzed during the current study are available from the corresponding authors on reasonable request.

Code availability
The code VOTCA is available from the gitlab repository, https://gitlab.mpcdf.mpg.de/votca/votca.git.

References
1. Venkatasubramanian, R., Siivola, E., Colpitts, T. & O'Quinn, B. Thin-film thermoelectric devices with high room-temperature figures of merit. *Nature* **413**, 597–602 (2001).
2. Lesne, E. et al. Highly efficient and tunable spin-to-charge conversion through Rashba coupling at oxide interfaces. *Nat. Mater.* **15**, 1261–1266 (2016).
3. Roberts, S. T. Energy transport: singlet to triplet and back again. *Nat. Chem.* **7**, 764–765 (2015).
4. Nielsen, C. B., Holliday, S., Chen, H.-Y., Cryer, S. J. & McCulloch, I. Non-fullerene electron acceptors for use in organic solar cells. *Acc. Chem. Res.* **48**, 2803–2812 (2015).
5. Collins, S. D., Ran, N. A., Heiber, M. C. & Nguyen, T.-Q. Small is powerful: recent progress in solution-processed small molecule solar cells. *Adv. Energy Mater.* **7**, 1602242 (2017).
6. Zhao, J. et al. Efficient organic solar cells processed from hydrocarbon solvents. *Nat. Energy* **1**, 15027 (2016).
7. Firdaus, Y. et al. Key parameters requirements for non-fullerene-based organic solar cells with power conversion efficiency >20%. *Adv. Sci.* **6**, 1802028 (2019).
8. Xu, X. et al. Single-junction polymer solar cells with 16.35% efficiency enabled by a platinum(II) complexation strategy. *Adv. Mater.* **31**, 1901872 (2019).
9. Lin, Y. et al. 17.1% efficient single-junction organic solar cells enabled by n-type doping of the bulk-heterojunction. *Adv. Sci.* **7**, 1903419 (2020).
10. Liu, Q. et al. 18% Efficiency organic solar cells. *Sci. Bull.* **65**, 272–275 (2020).
11. Khan, J. I. et al. Impact of acceptor quadrupole moment on charge generation and recombination in blends of IDT-based non-fullerene acceptors with PCE10 as donor polymer. *Adv. Energy Mater.* **11**, 2100839 (2021).
12. Li, C. et al. Non-fullerene acceptors with branched side chains and improved molecular packing to exceed 18% efficiency in organic solar cells. *Nat. Energy* **6**, 605–613 (2021).
13. Qin, J. et al. A chlorinated copolymer donor demonstrates a 18.13% power conversion efficiency. *J. Semiconductors* **42**, 010501 (2021).
14. Zhan, L. et al. Layer-by-layer processed ternary organic photovoltaics with efficiency over 18%. *Adv. Mater.* **33**, 2007231 (2021).
15. Jin, K., Xiao, Z. & Ding, L. D18, an eximious solar polymer! *J. Semiconductors* **42**, 010502 (2021).
16. Cui, Y. et al. Over 16% efficiency organic photovoltaic cells enabled by a chlorinated acceptor with increased open-circuit voltages. *Nat. Commun.* **10**, 1–8 (2019).
17. Bao, S. et al. Volatilizable solid additive-assisted treatment enables organic solar cells with efficiency over 18.8% and fill factor exceeding 80%. *Adv. Mater.* **33**, 2105301 (2021).
18. Li, M. et al. Solution-processed organic tandem solar cells with power conversion efficiencies \textgreater12%. *Nat. Photonics* **11**, 85–90 (2017).
19. Scharber, M. C. et al. Design rules for donors in bulk-heterojunction solar cells—towards 10 % energy-conversion efficiency. *Adv. Mater.* **18**, 789–794 (2006).
20. Blakesley, J. C. & Neher, D. Relationship between energetic disorder and open-circuit voltage in bulk heterojunction organic solar cells. *Phys. Rev. B* **84**, 075210 (2011).
21. Garcia-Belmonte, G. & Bisquert, J. Open-circuit voltage limit caused by recombination through tail states in bulk heterojunction polymer-fullerene solar cells. *Appl. Phys. Lett.* **96**, 113301 (2010).
22. Blakesley, J. C. & Greenham, N. C. Charge transfer at polymer-electrode interfaces: the effect of energetic disorder and thermal injection on band bending and open-circuit voltage. *J. Appl. Phys.* **106**, 034507 (2009).
23. Collins, S. D., Proctor, C. M., Ran, N. A. & Nguyen, T.-Q. Understanding open-circuit voltage loss through the density of states in organic bulk heterojunction solar cells. *Adv. Energy Mater.* **6**, 1501721 (2016).

24. Neher, D., Kniepert, J., Elimelech, A. & Koster, L. J. A. A new figure of merit for organic solar cells with transport-limited photocurrents. *Sci. Rep.* **6**, 24861 (2016).

25. Würfel, U., Neher, D., Spies, A. & Albrecht, S. Impact of charge transport on current–voltage characteristics and power-conversion efficiency of organic solar cells. *Nat. Commun.* **6**, 6951 (2015).

26. Sandberg, O. J. & Armin, A. Energetics and kinetics requirements for organic solar cells to break the 20% power conversion efficiency barrier. *J. Phys. Chem. C* **125**, 15590–15598 (2021).

27. Nolasco, J. C. et al. Understanding the open circuit voltage in organic solar cells on the basis of a donor-acceptor abrupt (p-n++) heterojunction. *Sol. Energy* **184**, 610–619 (2019).

28. Poelking, C. et al. Impact of mesoscale order on open-circuit voltage in organic solar cells. *Nat. Mater.* **14**, 434–439 (2014).

29. Poelking, C. & Andrienko, D. Design rules for organic donor-acceptor heterojunctions: pathway for charge splitting and detrapping. *J. Am. Chem. Soc.* **137**, 6320–6326 (2015).

30. D'Avino, G. et al. Electrostatic phenomena in organic semiconductors: fundamentals and implications for photovoltaics. *J. Phys.: Condensed Matter* **28**, 433002 (2016).

31. Schwarze, M. et al. Impact of molecular quadrupole moments on the energy levels at organic heterojunctions. *Nat. Commun.* **10**, 1–9 (2019).

32. Karuthedath, S. et al. Intrinsic efficiency limits in low-bandgap non-fullerene acceptor organic solar cells. *Nat. Mater.* **20**, 378–384 (2021).

33. Markina, A. et al. Chemical design rules for non-fullerene acceptors in organic solar cells. advanced energy materials. *Adv. Energy Mater.* **11**, 2102363 (2021).

34. Forero-Martinez, N. C., Lin, K.-H., Kremer, K. & Andrienko, D. Virtual screening for organic solar cells and light emitting diodes. *Adv. Sci.* **9**, 2200825 (2022).

35. Schwarze, M. et al. Band structure engineering in organic semiconductors. *Science* **352**, 1446–1449 (2016).

36. D'Avino, G., Muccioli, L., Olivier, Y. & Beljonne, D. Charge separation and recombination at polymer–fullerene heterojunctions: delocalization and hybridization effects. *J. Phys. Chem. Lett.* **7**, 536–540 (2016).

37. Poelking, C. & Andrienko, D. Long-range embedding of molecular ions and excitations in a polarizable molecular environment. *J. Chem. Theory Comput.* **12**, 4516–4523 (2016).

38. Vandewal, K., Tvingstedt, K., Gadisa, A., Inganäs, O. & Manca, J. V. Relating the open-circuit voltage to interface molecular properties of donor:acceptor bulk heterojunction solar cells. *Phys. Rev. B* **81**, 125204 (2010).

39. Burke, T. M., Sweetnam, S., Vandewal, K. & McGehee, M. D. Beyond Langevin recombination: how equilibrium between free carriers and charge transfer states determines the open-circuit voltage of organic solar cells. *Adv. Energy Mater.* **5**, 1500123 (2015).

40. Banerjee, R. et al. Evidence for kinetically limited thickness dependent phase separation in organic thin film blends. *Phys. Rev. Lett.* **110**, 185506 (2013).

41. Schünemann, C. et al. Phase separation analysis of bulk heterojunctions in small-molecule organic solar cells using zinc-phthalocyanine and C_{60}. *Phys. Rev. B* **85**, 245314 (2012).

42. Rühle, V., Junghans, C., Lukyanov, A., Kremer, K. & Andrienko, D. Versatile object-oriented toolkit for coarse-graining applications. *J. Chem. Theory Comput.* **5**, 3211–3223 (2009).

43. Rühle, V. et al. Microscopic simulations of charge transport in disordered organic semiconductors. *J. Chem. Theory Comput.* **7**, 3335–3345 (2011).

44. Benduhn, J. et al. Intrinsic non-radiative voltage losses in fullerene-based organic solar cells. *Nat. Energy* **2**, 1–6 (2017).

45. Xing, S. et al. Miniaturized VIS-NIR spectrometers based on narrowband and tunable transmission cavity organic photodetectors with ultrahigh specific detectivity above 1014 Jones. *Adv. Mater.* **33**, 2102967 (2021).

Author contributions

C.P. performed simulations and prepared the first draft of the manuscript. J.B., D.S., M.S., S.R., F.P. performed experiments and contributed to manuscript writing. D.A. supervised the computational part of the work and contributed to the manuscript. K.V., K.L., and D.N. conceived the study, supervised the experiments and data analysis, and contributed to the manuscript. All authors contributed to the revision of the final version of the manuscript.

Competing interests

The authors declare no competing interests.

Additional information

Supplementary information The online version contains supplementary material available at https://doi.org/10.1038/s42005-022-01084-x.

Correspondence and requests for materials should be addressed to Koen Vandewal or Denis Andrienko.

Peer review information *Communications Physics* thanks Jairo Nolasco and the other, anonymous, reviewer(s) for their contribution to the peer review of this work. Peer reviewer reports are available.

Reprints and permission information is available at http://www.nature.com/reprints

Publisher's note Springer Nature remains neutral with regard to jurisdictional claims in published maps and institutional affiliations.